THE ASTROPHYSICAL JOURNAL, 461:38–54, 1996 April 10

THE OPTICAL REDSHIFT SURVEY. II. DERIVATION OF THE LUMINOSITY AND DIAMETER FUNCTIONS AND OF THE DENSITY FIELD[1]

BASÍLIO X. SANTIAGO,[2] MICHAEL A. STRAUSS,[3] OFER LAHAV,[2] MARC DAVIS,[4]
ALAN DRESSLER,[5] AND JOHN P. HUCHRA[6]

Received 1995 July 18; accepted 1995 October 12

ABSTRACT

We quantify the effects of Galactic extinction on the derived luminosity and diameter functions and on the density field of a redshift sample. Galaxy magnitudes are more affected by extinction than are diameters, although the effect on the latter is more variable from galaxy to galaxy, making it more difficult to quantify. We develop a maximum likelihood approach to correct the luminosity function, the diameter function, and the density field for extinction effects. The effects of random and systematic photometric errors are also investigated. The derived density field is robust to both random and systematic magnitude errors as long as these are uncorrelated with position on the sky since biases in the derived selection function and number counts tend to cancel one another. Extinction-corrected luminosity and diameter functions are derived for several subsamples of the Optical Redshift Survey (ORS). Extinction corrections for the diameter-limited subsamples are found to be unreliable, possibly due to the superposition of random and systematic errors. The ORS subsamples are combined using overall density scaling factors from a full-sky redshift survey of *IRAS* galaxies, allowing the reconstruction of the optical galaxy density field over most of the sky to 8000 km s^{-1}.

Subject headings: dust, extinction — galaxies: distances and redshifts — galaxies: fundamental parameters — galaxies: luminosity function, mass function — galaxies: photometry

1. INTRODUCTION

Santiago et al. (1995, hereafter Paper I) presented the Optical Redshift Survey (ORS).

The ORS contains ~8500 galaxies with almost complete redshift information, selected from the Uppsala General Catalogue (UGC; Nilson 1973), the European Southern Observatory Catalog (ESO; Lauberts & Valentijn 1989), and the Extension to the Southern Galaxies Catalogue (ESGC; Corwin & Skiff 1995). The sample covers most of the sky with $|b| > 20°$ in both hemispheres, and consists of two largely overlapping subsamples, limited in apparent magnitude and diameter, respectively. This sample is used to derive the galaxy density field to $cz \approx 8000$ km s^{-1} and, in future papers in this series, to study its dependence on galaxy morphology and spectral properties. Its dense sampling and large variety in galaxy content make the ORS ideal for this purpose. Nevertheless, since there is no single optical galaxy catalog covering the entire sky that probes significantly beyond the Local Supercluster, the ORS sample selection is based on three different catalog and thus is not uniform over the sky. There may also be systematic trends in the magnitude and diameter scales internal to the different galaxy catalog from which ORS was derived. In addition, the ORS extends to low Galactic latitudes where variable Galactic absorption introduces an additional source of systematic variations in the sample selection. Previous studies of the large-scale distribution of galaxies have either worked in passbands where Galactic extinction was unimportant (e.g., Strauss et al. 1990) or have restricted themselves to regions of the sky in which the measured extinction was low (e.g., da Costa et al. 1994; cf. Appendix A of Strauss et al. 1992b). In this paper, our aim is to measure the density field of galaxies in the face of extinction and photometric errors; this paper describes our techniques for doing so, and our tests of these methods.

Recovering the galaxy density field requires determining the correct selection function for the sample. The selection function quantifies the loss of galaxies due to the magnitude or diameter limit and to any other selection effect that may be present. Thus, nonuniformities in survey sampling must be correctly incorporated by the derived selection function. The selection function is also intimately related to the galaxy luminosity and diameter functions in magnitude or diameter-limited surveys, respectively. The latter are cosmologically relevant quantities; their shape and dependence on environment density or on galaxy intrinsic properties have the potential to constrain different scenarios of structure formation (Blumenthal et al. 1984; White & Frenk 1991; Cole et al. 1994). A precise determination of the luminosity function and diameter function at $z = 0$ is necessary when studying the evolution of these functions or when comparing observed galaxy number counts with model predictions (Davis, Geller, & Huchra 1978; Dekel & Rees 1987; Koo & Kron 1992). Previous determinations of the luminosity function of optical galaxies have been carried out by Kirshner, Oemler, & Schechter (1979), Sandage,

---

[1] Based in part on data obtained at Lick Observatory, operated by the University of California; the Multiple Mirror Telescope, a joint facility of the Smithsonian Astrophysical Observatory and the University of Arizona; Cerro Tololo Inter-American Observatory, operated by the Association of Universities for Research in Astronomy, Inc., under contract with the National Science Foundation; Palomar Observatory, operated by the California Institute of Technology, the Observatories of the Carnegie Institution, and Cornell University; and Las Campanas Observatory, operated by the Observatories of the Carnegie Institution.

[2] Institute of Astronomy, Cambridge University, Madingley Road, Cambridge CB3 0HA, UK.

[3] Institute for Advanced Study, School of Natural Sciences, Princeton, NJ 08540.

[4] Physics and Astronomy Departments, University of California, Berkeley, CA 94720.

[5] Observatories of the Carnegie Institution of Washington, 813 Santa Barbara Street, Pasadena, CA 91101.

[6] Center for Astrophysics, 60 Garden Street, Cambridge, MA 02138.

Tammann, & Yahil (1979), Davis & Huchra (1982), Kirshner et al. (1983), Efstathiou, Ellis, & Peterson (1988), de Lapparent, Geller, & Huchra (1989), Santiago & Strauss (1992), Loveday et al. (1992, 1995), and Marzke, Geller, & Huchra (1994), among others. Different parametric and nonparametric methods for determining the luminosity function and diameter function have been developed and applied; these methods are unbiased by the presence of inhomogeneities in the galaxy distribution (Turner 1979; Sandage et al. 1979; Nicoll & Segal 1983; Choloniewski 1986; Efstathiou et al. 1988. See Binggeli, Sandage, & Tammann 1988 for a review). The diameter function has been investigated by Maia & da Costa (1990); Lahav, Rowan-Robinson, & Lynden-Bell (1988); and Hudson & Lynden-Bell (1991). Finally, the bivariate distribution of diameters and absolute magnitudes has been analyzed by Choloniewski (1985), and Sodré & Lahav (1993).

In this paper we discuss the effects of Galactic absorption and systematic and random magnitude or diameter errors on the derived selection function and density field. In § 2, we quantify the extinction effects by means of Monte Carlo simulations. A maximum likelihood method is derived to recover an unbiased estimate of the selection function and of the density field. The influence of other systematic and random errors is also addressed. In § 3, we apply the methods developed in § 2 in order to recover the ORS luminosity and diameter functions. Our main conclusions are presented in § 4. Throughout this paper, we work in redshift space; thus we are not concerned here about corrections from redshift to real space for galaxies in redshift surveys.

2. EXTINCTION AND SYSTEMATIC AND RANDOM ERRORS

2.1. *The Selection Function and Galactic Extinction*

Any magnitude or diameter-limited sample will become sparser at larger redshifts due to the increasing loss of galaxies caused by the adopted apparent magnitude or diameter cutoff. This effect is quantified by the selection function which expresses the fraction of the total population of galaxies that are expected to satisfy the sample's selection criterion. In the case of a flux-limited sample, the selection function is given by

$$\phi(r) = \frac{\int_{L_{\min}(r)}^{\infty} \Phi(L)dL}{\int_{L_s}^{\infty} \Phi(L)dL} , \tag{1}$$

where $L_{\min}(r) \equiv 4\pi r^2 f_{\min}$ is the minimum luminosity necessary for a galaxy at distance r to make it into the sample, $f_{\min}$ is the limiting flux[7] of the sample in ergs s^{-1} cm^{-2}, and $\Phi(L)$ is the luminosity function in the passband in which the survey is done. In principle, the lower limit of the integral in the denominator should be zero, but we set it to a small value $L_s \equiv L_{\min}(r_s)$, as it is impossible in practice to quantify the faintest end of the luminosity function. We set $r_s = 500$ km s^{-1} in what follows. In the equation above and throughout this paper we assume that $\Phi(L)$ is universal, showing no dependence on location in the universe. We will test this assumption a posteriori in § 3.

Yahil et al. (1991, hereafter YSDH) adopt a simple parameterized form for the selection function, characterized by three numbers, which experience has shown is sufficiently general for these purposes (e.g., Santiago & Strauss 1992):

$$\phi(r) = \begin{cases} \left(\frac{r}{r_s}\right)^{-2\alpha}\left(\frac{r_*^2 + r^2}{r_* + r_s^2}\right)^{-\beta} , & r > r_s , \\ 1 , & r \leq r_s . \end{cases} \tag{2}$$

Equation (1) implies that the luminosity function can be related to the selection function by a derivative, yielding

$$\Phi(L) = C\left(\frac{\alpha}{L} + \frac{\beta}{L_* + L}\right)\left(\frac{L}{L_*}\right)^{-\alpha}\left(1 + \frac{L}{L_*}\right)^{-\beta} , \tag{3}$$

where α, β, and $L_* \equiv 4\pi r_*^2 f_{\min}$ are free parameters and C is a normalization constant. Thus r_* is the distance at which galaxies at the survey flux limit have a luminosity characteristic of that of the knee of the luminosity function. The best-fit values for these parameters are given below in § 3. This form is a generalization of the Schechter (1976) function with one additional free parameter (cf. Yahil 1988). We will use the parameterization of equation (2) in this paper, but equation (1) will have to be generalized to reflect the effects of extinction. Before doing so, let us remind ourselves how one would solve for the selection function for the sample in the case of no extinction. Following YSDH, we maximize the likelihood Λ, the product of probabilities p that each galaxy has its measured luminosity, given its redshift. For a purely flux-limited sample, without the effects of extinction, this is

$$\begin{aligned} \Lambda &= \prod_i^N p(L_i \mid r_i) \\ &= \prod_i^N \left[\Phi(L_i) \Big/ \int_{L_{\min}(r_i)}^{\infty} \Phi(L')dL' \right] \\ &\propto \prod_i^N \frac{1}{\phi(r_i)} \left.\frac{d\phi(r)}{dr}\right|_{r_{\max}(L_i)} , \end{aligned} \tag{4}$$

where N is the total number of galaxies in the sample and $r_{\max} \equiv r(f/f_{\min})^{1/2}$ is the maximum distance out to which the galaxy could be placed and remain in the sample. The last step follows from equation (1).

The derived selection function is used for recovering the density field; the sampling selection effect is compensated by weighting each galaxy by the inverse of the selection function at its position, $w_i = 1/\phi(r_i)$, $i = 1, \ldots, N$. Densities can then be computed by summing each galaxy's contribution within a given volume and dividing by that volume. We usually express densities in units of the global mean density

$$n_1 = \sum_i w_i/V , \tag{5}$$

computed over the entire sample volume V out to some limiting redshift (see YSDH, eqs. [13]–[15]).

Now let us consider the effects of extinction. Consider a galaxy whose intrinsic apparent photographic B magnitude is given by m. If the galaxy lies in the direction (l, b), its observed magnitude is given by

$$m_{\text{obs}} = m + \gamma_m A_B(l, b) , \tag{6}$$

where $A_B(l, b)$ is the extinction in the given direction and passband. If m_{obs} is the total observed magnitude, $\gamma_m = 1$; extinction simply reduces the surface brightness at each point on the galaxy's two-dimensional figure by $A_B(l, b)$. For isophotal magnitudes, however, not only does every point in the galaxy become dimmer, but the radius of the isophote

---

[7] In the case of a survey limited in magnitudes to m_{lim}, $f_{\min} \propto 10^{-0.4 m_{\text{lim}}}$.

shrinks, and thus we expect $\gamma_m > 1$, the exact value depending on the two-dimensional light profile of the object (Cameron 1990). For example, the effects of extinction for a spiral disk with an exponential light profile of e-folding length θ_e can be calculated analytically. The observed isophotal diameter $\theta_{\rm obs}$ is related to the intrinsic isophotal diameter θ by

$$\theta_{\rm obs} = \theta - 0.921\theta_e A_B\ . \tag{7}$$

The quantity γ_m as defined in equation (5) is then

$$\gamma_m = 1 + \frac{2.5}{A_B}\log\frac{1 - e^{-x}(1 + x)}{1 - e^{-x_{\rm obs}}(1 + x_{\rm obs})} \approx \frac{1 - e^{-x}}{1 - e^{-x}(1 + x)}\ , \tag{8}$$

where $x \equiv \theta/\theta_e$ and $x_{\rm obs} \equiv \theta_{\rm obs}/\theta_e$ are the number of scale lengths subtended by the intrinsic and observed diameters, respectively. The second equality holds in the limit of small A_B. Notice that the second term on the right-hand side of equation (8) depends on the profile shape through the number of e-folding lengths within θ and $\theta_{\rm obs}$.

We can similarly define a quantity γ_d which gives the fractional decrease in isophotal diameter with extinction:

$$\gamma_d \equiv \frac{5}{A_B}\log\frac{\theta}{\theta_{\rm obs}} \approx \frac{2.0}{x}\ , \tag{9}$$

where again the second equality holds in the limit of small A_B.

For a given surface brightness profile, the quantities γ_m and γ_d depend only on x and A_B. They are related to the fractional changes in flux and diameters by the equations $\delta f/f = 1 - 10^{-0.4A_B\gamma_m}$ and $\delta\theta/\theta = 1 - 10^{-0.2A_B\gamma_d}$, respectively. Figure 1 shows γ_d and γ_m as a function of θ/θ_e for $A_B = 0.3$ mag; the dependence on A_B is weak for small and moderate A_B. Panel *a* assumes an exponential disk, and panel *b* refers to a de Vaucouleurs profile for which expressions analogous to equations (7)–(9) can be derived. In the latter case, γ_m also depends weakly on θ_e; we assumed a typical value for early-type galaxies. In both panels, the horizontal bars indicate the observed range of θ/θ_e values for disk and bulge galaxies, assuming limiting isophotal levels for detection characteristic of the ESO and Palomar plates. Note that γ_m is significantly larger than γ_d for any value of θ/θ_e; fluxes are more affected by extinction than are diameters. However, γ_d is a stronger function of x than is γ_m, since γ_d approaches 0 for large extinction, while γ_m approaches 1. Thus the approximation we will use of a single value of γ for an entire sample is likely to be less appropriate for diameter-limited samples than for magnitude-limited samples.

For a flux-limited sample, the effect of Galactic obscuration is to introduce a nonuniform, direction-dependent selection effect: the effective magnitude cutoff limit for a galaxy lying in the direction (l, b) is given by $m_{\rm lim} = m_{\rm lim,observed} - \gamma_m A_B(l, b)$ where $m_{\rm lim,observed} \equiv {\rm const} - 2.5 \log f_{\rm min}$ is the magnitude corresponding to the flux limit. In terms of the selection function, we now have

$$\phi_{\rm obs}[r, \gamma_m A_B(l, b)] = \frac{\int_{L_{\rm min}(r,\gamma_m A_B)}^{\infty} \Phi(L)dL}{\int_{L_s}^{\infty} \Phi(L)dL}\ , \tag{10}$$

where $L_{\rm min}(r, \gamma_m A_B) \equiv 4\pi r^2 f_{\rm min} \times 10^{0.4\gamma_m A_B}$ is the minimum luminosity necessary for a galaxy in this direction to make it into the sample. A similar expression holds for diameter-limited samples.

In the absence of absorption $[A_B(l, b) = 0]$, equation (10) becomes the usual definition of the selection function, $\phi(r)$ (eq. [1]), showing no dependence on direction in the sky. We call this quantity the intrinsic selection function $\phi(r)$, in order to distinguish it from the selection function that incorporates extinction, $\phi_{\rm obs}(r, \gamma A_B)$. The two functions are related by the equation

$$\phi_{\rm obs}(r, \gamma A_B) = \phi(r \times 10^{0.2\gamma A_B})\ . \tag{11}$$

Notice that it is ϕ rather than $\phi_{\rm obs}$ that is directly related to $\Phi(L)$ via equation (1). On the other hand, it is $\phi_{\rm obs}$ that quantifies the extinction selection effects inherent to the

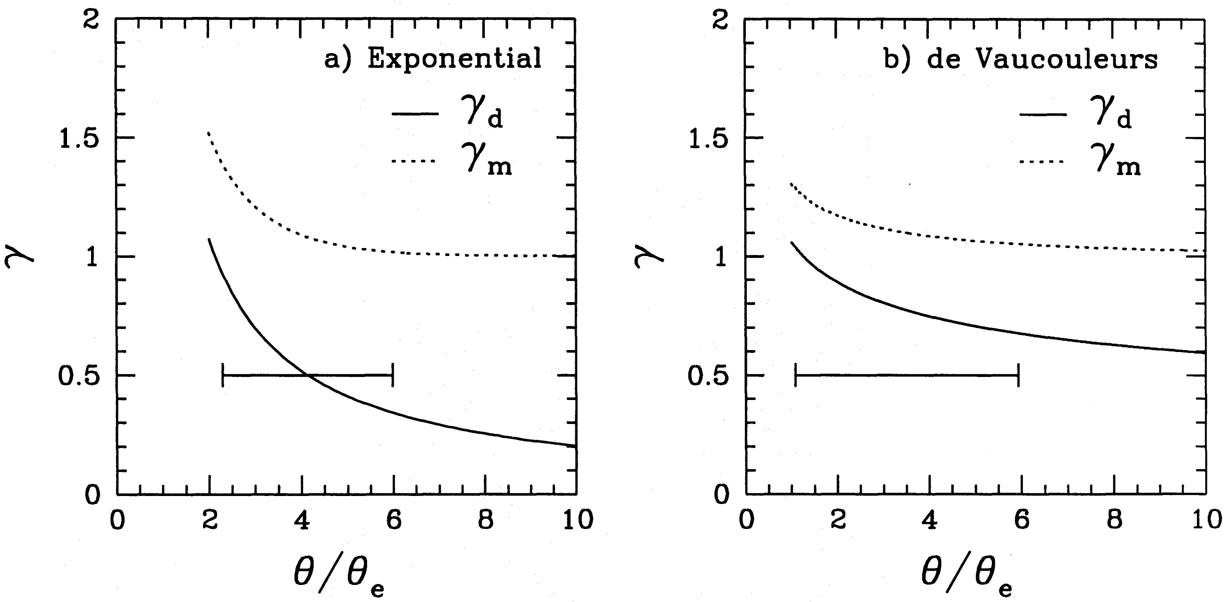

FIG. 1.—Values of γ associated with fluxes (γ_m; *dotted line*) and diameters (γ_d, *solid line*) for objects whose light profile is an exponential and which are subject to an extinction of $A_B = 0.3$ mag. We show γ as a function of the number of e-folding lengths θ/θ_e. The horizontal bars give the typical observed range of e-folding lengths for ORS galaxies. (*b*) As in (*a*), but for a de Vaucouleurs profile. In this case, θ_e is the de Vaucouleurs radius.

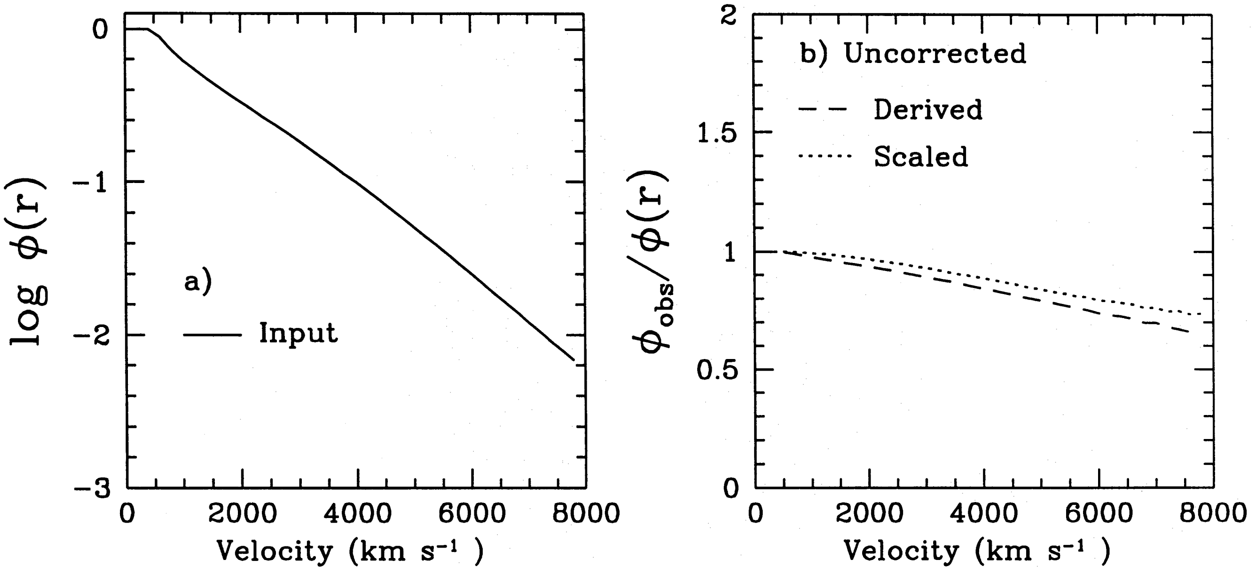

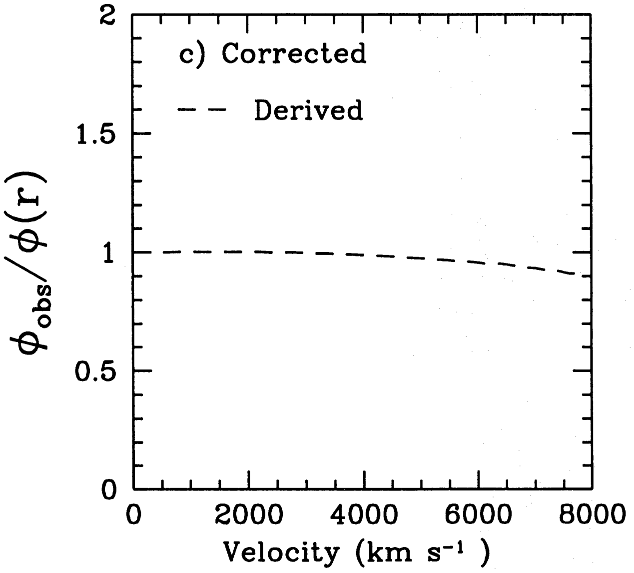

FIG. 2.—Input selection function $\phi(r)$ used for the Monte Carlo simulations in this paper. Note the logarithmic abscissa. (*b*) Effect of Galactic absorption on the selection function. The dashed line represents the ratio of the derived to the input selection function when extinction is completely ignored, in a simulation with $\langle\gamma\rangle = 1$ and extinctions drawn from Burstein & Heiles (1982). The dotted line is the selection function ratio, where the selection has been scaled using the mean A_B value in eq. (11). Note the linear scale. (*c*) Ratio of the selection function derived taking extinction into account, to ϕ.

sample. We thus need $\phi(r)$ to derive the luminosity function, and $\phi_{\rm obs}$ to derive an unbiased density field.

What are the errors resulting from not taking Galactic absorption into account when deriving the selection function and density field? We answer this question by means of simulations of a redshift survey. We use a standard cold dark matter (CDM) N-body simulation ($\Omega = 1$, $h = 0.5$, $\Lambda = 0$) generated by Karl Fisher, and select a random subsample of points around an origin chosen to represent the observer, according to an input selection function. Our results on the effect of extinction do not depend on the details of the cosmological model or selection function adopted. Fluxes are assigned to each selected point following the luminosity function consistent with the chosen intrinsic selection function. A "Galactic" coordinate system is set up as well, and each magnitude is attenuated according to the Burstein-Heiles (1982) extinction in that direction. The value of γ used for each point is drawn from a Gaussian distribution with mean unity and dispersion $\sigma = 0.2$. We thus allow for variations in the extinction correction from object to object, and uncertainties in the extinction map. The sample was then cut at $m_{\rm obs} \leq 14.5$. At this point, we wish to search for biases in our techniques for correcting for extinction, as opposed to assessing random errors in the derived quantities, and thus we have generated a random catalog with over 10,000 points, roughly twice that of the ORS sample itself.

We first compute the selection function for the sample without attempting to apply any correction for extinction effects; we make straight use of the method described in YSDH and outlined above. The input $\phi(r)$ used in this and all subsequent Monte Carlo experiments in this paper is shown in Figure 2*a*. The ratio of the derived to the input selection function is shown in Figure 2*b* as a dashed line. The monotonic decrease in the ratio is caused by the loss of galaxies from the sample due to Galactic absorption. However, this discrepancy is due mainly to the mean extinction over the sample; it is not sensitive to the variation of the extinction from point to point. The dotted line in Figure 2*b* is the quantity $\phi_{\rm obs}/\phi(r)$, where $\phi_{\rm obs}$ was calculated from equation (11), using the input selection function and the mean A_B taken over all the points in the simulation. This scaled selection function is very similar to the one derived directly from the sample.

It is the intrinsic selection function $\phi(r)$ that we are interested in recovering. We can generalize the maximum ikelihood expressions of equation (4) to take extinction into account:

$$\begin{aligned}\Lambda &= \prod_i^N p(L_i \,|\, r_i,\, \gamma_i A_B^i) \\ &= \prod_i^N \left[\Phi(L_i\, 10^{0.4\gamma_i A_B^i}) \middle/ \int_{L_{\min}(r_i,\, \gamma_i A_B^i)}^{\infty} \Phi(L')dL' \right] \\ &= \prod_i^N \frac{1}{\phi(10^{0.2\gamma_i A_B^i} r_i)} \left.\frac{d\phi(r)}{dr}\right|_{{\rm dex}(0.2\gamma_i A_B^i) r_{\max}(L_i)} , \qquad (12)\end{aligned}$$

where N is the total number of galaxies in the sample.

Equation (12) takes extinction directly into account when fitting for the parameters of $\phi(r)$. However, we do not have a priori knowledge of the values of γ_i, $i = 1, \ldots, N$. This would require knowing the surface brightness profiles of all galaxies in the sample. We thus make the approximation of a single value of γ for all galaxies as if they all had the same surface brightness profile; γ is then treated as an additional parameter to be fitted simultaneously to the luminosity (or selection) function. In Figure 2*c* we show the result of maximizing this new likelihood function for the same Monte Carlo simulation as in Figure 2*b*. The derived selection function is now in very good agreement with the input one. Given the intrinsic selection function, $\phi_{\rm obs}(r, \gamma A_B)$ for each galaxy follows directly from equation (11). Thus, this approach allows us to successfully recover the correct luminosity function (free of extinction biases) for a redshift sample, even in the presence of moderate variations in the true value of γ from galaxy to galaxy.

We next tested our ability to measure γ itself. We carried out a series of simulations in which the true mean value of γ was varied; in each case, the value of γ for each galaxy followed from a Gaussian distribution with a dispersion of 0.2. Figure 3*a* shows the derived γ-values as a function of the mean input γ. The filled symbols were derived from simulations of size similar to that used in Figure 2, containing about 10,000 points. The open symbols were obtained from simulations whose sizes are comparable to the ORS subsamples used in § 3 and that had random magnitude errors (typically of 0.5 mag) added to the extinction effect. Formal error bars from the maximum likelihood fits are plotted; the smaller simulations have larger error bars, as expected. The agreement between derived and input γ-values is still good in all cases, although there is a small trend toward underestimating large input γ for the small sample. We investigated the origin of this trend by plotting the derived selection functions (normalized to the input one) for each ORS-sized simulation in Figure 3*b*. Contrary to the error-free case, $\phi(r)$ is now shallower than the input function used (ratio greater than unity). This is caused by Malmquist bias, as will be explained in § 2.3. Notice, however, that the amplitude of the bias in $\phi(r)$ is insensitive to γ, indicating that the trend in γ seen in Figure 3*a* does not lead to discrepant best-fit solutions for $\phi(r)$. Instead, the systematics in γ just compensate for similar biases in the $\phi(r)$ parameters; indeed, the derived density field (using the methods discussed in connection with Fig. 5*a* below) shows no systematic bias that grows with γ. We thus conclude that our revised likelihood approach recovers the right $\phi(r)$ (apart from Malmquist bias) even when γ is significantly different from unity and in the presence of random scatter in the magnitudes.

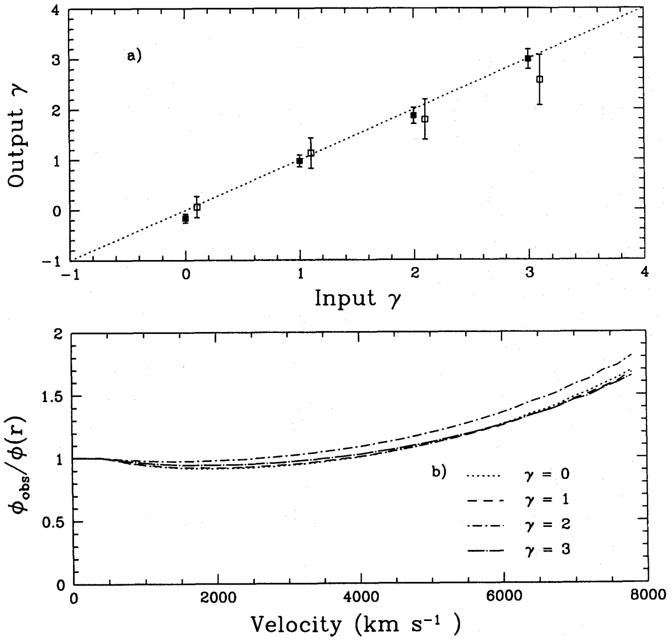

FIG. 3.—(*a*) Relation between the input and derived values of the extinction correction parameter γ from Monte Carlo simulations. Filled symbols correspond to samples containing over 10,000 galaxies. Open symbols refer to samples comparable in size to the ORS subsamples discussed in § 3 (about 2000 galaxies). Error bars are the formal uncertainties from the maximum likelihood fit. (*b*) Ratio of derived to input selection function for the ORS-sized simulations whose observed and input γ-values are given by the open symbols in (*a*).

We now consider the effect Galactic absorption has on the derived density field. We again use the Monte Carlo simulation with input mean $\gamma = 1$. Galaxies are weighted by the inverse of the derived selection function, $\phi_{\rm obs}(r, \gamma A_B)$, and smoothed with a top hat of radius given by the mean interparticle separation at each point. Densities $\rho(\boldsymbol{r})$ are measured on a grid of points in space, interspaced by the mean interparticle distance at their location. We normalize the densities by n_1 as given by equation (5), the global mean computed over the whole sample volume to 8000 km s^{-1}, and define deviations from the mean as $\delta(\boldsymbol{r}) \equiv \rho(\boldsymbol{r})/\langle\rho\rangle - 1$.

Figure 4 shows how these grid-point normalized densities, $\delta(\boldsymbol{r})$, are affected by Galactic absorption. In Figure 4*a* we plot the errors in the density, $\Delta\delta(\boldsymbol{r}) \equiv \delta(\boldsymbol{r}) - \delta_{\rm obs}(\boldsymbol{r})$, as a function of A_B. The quantity $\delta_{\rm obs}(\boldsymbol{r})$ was computed by weighting each galaxy by the inverse of the selection function which completely ignores extinction (Fig. 2*b*). We show the mean value of $\Delta\delta$ for different bins in A_B (*solid line*). There is clearly a trend in the sense that densities are underestimated (overestimated) in regions of high (low) absorption. This is a direct consequence of the insensitivity of the selection function to variations in extinction over the sky. In Figure 4*b*, $\Delta\delta$ is plotted as a function of redshift. The mean over all points in each distance bin is again plotted as a solid line. Also plotted are the mean curves for the points in each bin with the 25% highest and lowest A_B values. Notice that $\Delta\delta$ for the upper quartile tends to increase with distance, whereas the lower quartile shows a systematic decrease: the bias in the density field caused by extinction increases with distance. This is consistent with the increasingly larger disagreement between the derived and input selection functions in Figure 2*b*. At $v \sim 4000$ km s^{-1}, the error in density can be as large as $\Delta\delta \sim 1.0$, although the typical values are around 0.2. The results shown are for $\langle\gamma\rangle = 1$; these effects become larger for larger values of γ. On the other hand, there is no systematic bias in the mean density at a given distance; at each distance, there will be directions with both high and low A_B values, whose densities are underestimated and overestimated, respectively. We thus conclude that ignoring extinction tends to cause biases only in local density estimates, while densities averaged over the solid angle of a survey are not systematically affected.

Finally, in Figure 4*c*, we show how the difference between intrinsic and derived densities behaves as a function of the intrinsic density itself. Again, no systematic trend is seen when all points are considered. However, for the high and

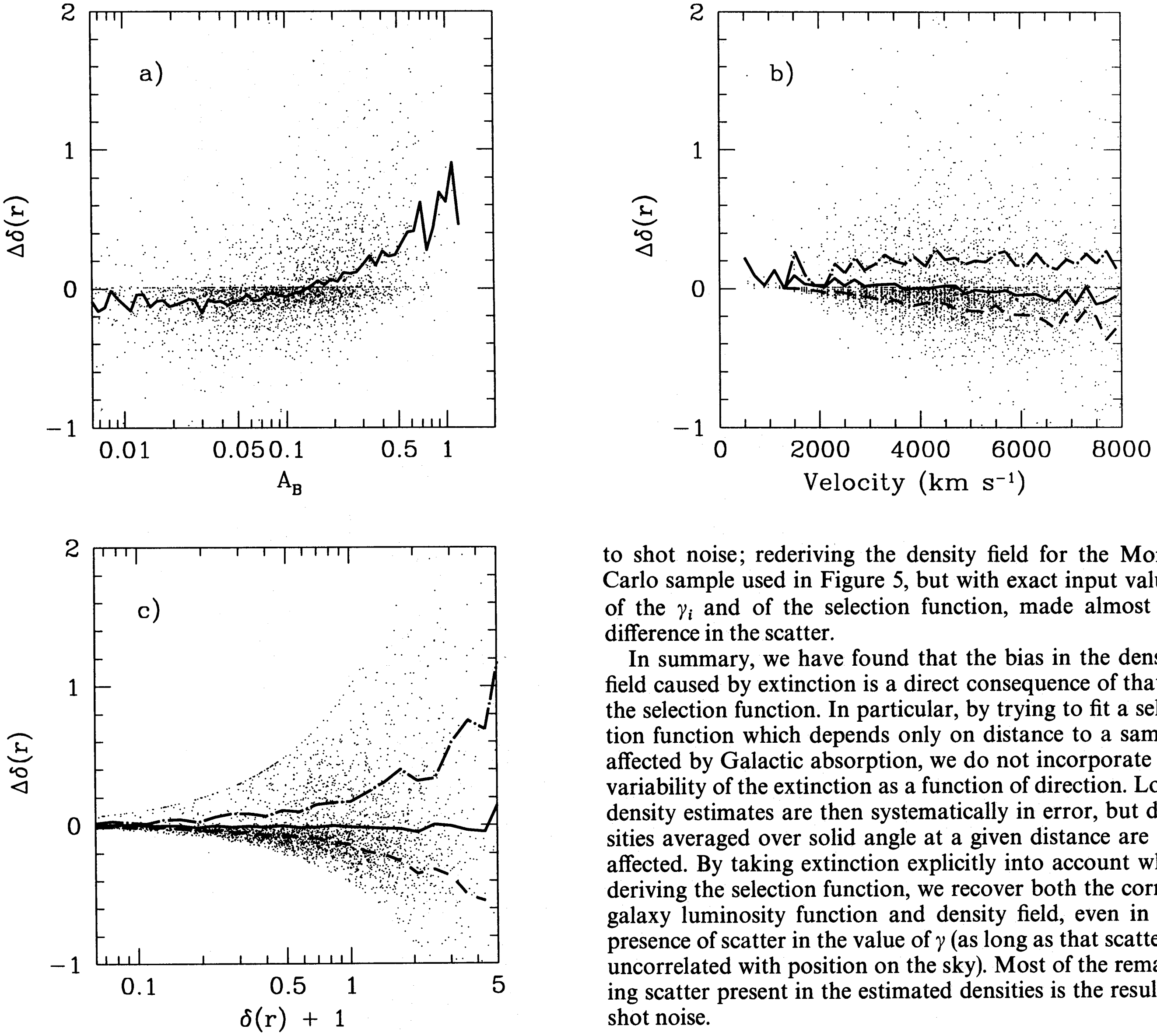

FIG. 4.—Effect of Galactic absorption on the derived density field. The three panels give the difference between the input and derived densities calculated on a grid of points for a Monte Carlo sample with input $\langle\gamma\rangle = 1$. The simulated galaxies were weighted by the inverse of the derived selection function given in Fig. 2*b*. For clarity, only every second point is plotted. (*a*) Density error as a function of A_B. The solid line is the mean error in each bin of A_B. (*b*) Density error as a function of distance. The solid line is the mean error in each bin of distance. The dashed line (dot-dashed line) is the mean error over the points with the 25% lowest (highest) A_B values. (*c*) As in (*b*), now as a function of the input density. The upper and lower envelopes in this case are due to the fact that both δ and $\delta_{\rm obs}$ have lower limits of -1.

low A_B quartiles, we see errors of about 20%–25% the mean density.

Figure 5 shows the results of weighting each galaxy by the inverse of $\phi_{\rm obs}(r, \gamma A_B)$ as derived by simultaneously fitting $\phi(r)$ and γ and then applying equation (11) to each object. No systematic error in the densities is now visible either as a function of A_B, distance, or intrinsic density. In particular, the mean curves for the highest and lowest extinction quartiles (Figs. 5*b* and 5*c*) are both very close to zero. In addition, the scatter in the diagrams has decreased substantially. The remaining scatter is almost entirely due to shot noise; rederiving the density field for the Monte Carlo sample used in Figure 5, but with exact input values of the γ_i and of the selection function, made almost no difference in the scatter.

In summary, we have found that the bias in the density field caused by extinction is a direct consequence of that in the selection function. In particular, by trying to fit a selection function which depends only on distance to a sample affected by Galactic absorption, we do not incorporate the variability of the extinction as a function of direction. Local density estimates are then systematically in error, but densities averaged over solid angle at a given distance are not affected. By taking extinction explicitly into account when deriving the selection function, we recover both the correct galaxy luminosity function and density field, even in the presence of scatter in the value of γ (as long as that scatter is uncorrelated with position on the sky). Most of the remaining scatter present in the estimated densities is the result of shot noise.

2.2. *Other Systematic Effects*

As far as their influence on the derived density field is concerned, systematic errors fall into two categories: position-dependent and position-independent errors. In the former case, without a priori information on the form of the error (such as we have in the form of the Burstein-Heiles maps in the case of extinction), one cannot solve or test for it. In the latter case, however, a fit to a radial selection function will absorb the systematic effect[8], leaving the derived density unbiased.

Consider, for instance, the case in which the observed magnitudes are incorrect by both an offset and a scale error (such as might be caused by uncorrected nonlinearities in photographic plate material):

$$m_{\rm obs} = am + b \, , \qquad (13)$$

where a and b are constants and m represents the true magnitude. The selection function that accommodates this kind of magnitude error is given by equation (1) with $L_{\rm min}(r) =$

---

[8] This is true to the extent that the functional form of the selection function to which we are fitting is sufficiently general to be able to absorb the systematic effect.

1996ApJ...461...38S

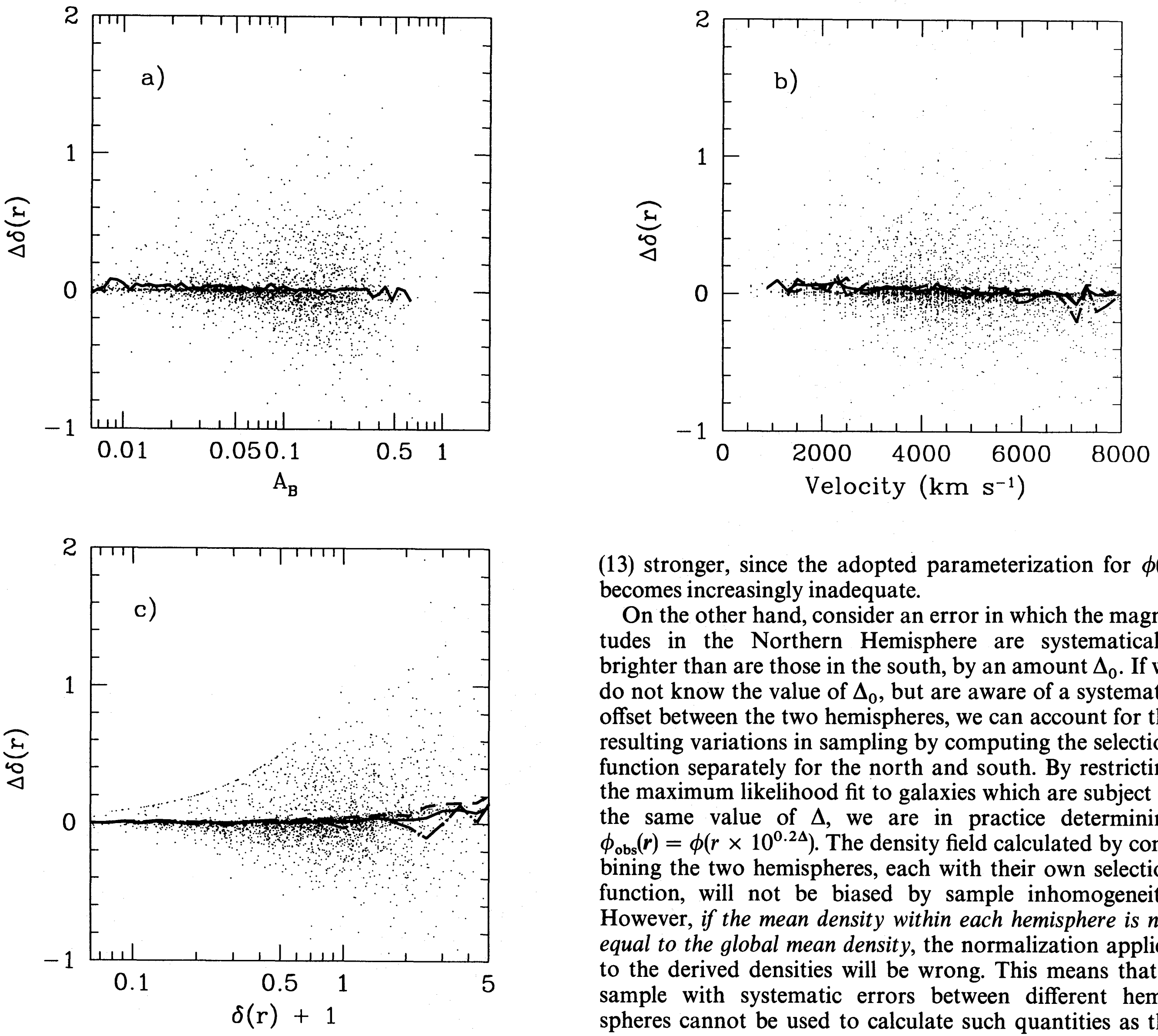

FIG. 5.—As in Fig. 4, with extinction properly corrected for in the density calculation.

$4\pi r^2 f_{\rm min}^{1/a} \times 10^{0.4b/a}$. Notice that both the selection function and the cutoff luminosity $L_{\rm min}$ are still functions of distance only. Our maximum likelihood method will thus find the correct selection function even in the presence of such systematic effects, as we demonstrate with a Monte Carlo simulation. Observed magnitudes were obtained from equation (13) with $a = 1.04$, $b = -0.3$, giving a systematic effect comparable to that of extinction. This simulation did not include the effects of extinction or random magnitude errors. The trend given by equation (13) is assumed unknown a priori, and as such is not explicitly corrected for when deriving $\phi(r)$. Figure 6*a* shows the ratio of derived to input selection functions. The former is steeper than the latter due to the loss of galaxies caused by the systematic trend in the magnitudes. The corresponding $\Phi(L)$ will be then equally biased. The derived density field, however, shows only a small bias, as a function of both distance (Fig. 6*b*) and intrinsic density (Fig. 6*c*). The residual bias increases if we make the systematic error given by equation (13) stronger, since the adopted parameterization for $\phi(r)$ becomes increasingly inadequate.

On the other hand, consider an error in which the magnitudes in the Northern Hemisphere are systematically brighter than are those in the south, by an amount Δ_0. If we do not know the value of Δ_0, but are aware of a systematic offset between the two hemispheres, we can account for the resulting variations in sampling by computing the selection function separately for the north and south. By restricting the maximum likelihood fit to galaxies which are subject to the same value of Δ, we are in practice determining $\phi_{\rm obs}(r) = \phi(r \times 10^{0.2\Delta})$. The density field calculated by combining the two hemispheres, each with their own selection function, will not be biased by sample inhomogeneity. However, *if the mean density within each hemisphere is not equal to the global mean density*, the normalization applied to the derived densities will be wrong. This means that a sample with systematic errors between different hemispheres cannot be used to calculate such quantities as the dipole moment of the galaxy distribution (e.g., Strauss et al. 1992c). In order to properly normalize the *global* density field in such a case, one needs external information in the density field, such as that supplied by the *IRAS* redshift survey (Strauss et al. 1992a; Fisher et al. 1995). This is the approach we use in § 3 below.

2.3. *Random Errors*

Random errors in the magnitudes have two effects on the derived density field in a magnitude-limited sample: first, galaxies scatter across the magnitude limit $m_{\rm lim}$. Because galaxies with true magnitudes fainter than $m_{\rm lim}$ outnumber those brighter than $m_{\rm lim}$, the net effect is to augment the numbers of galaxies over the case of no errors, an effect which increases with distance. Second, the magnitude errors convolve directly with the luminosity function to broaden it, thus making the selection function shallower. These two effects work in opposite senses, and thus we might hope that they largely cancel one another in the density field. Let the distribution of errors ϵ in the fluxes be $g(\epsilon, f)$, where the distribution can depend on f itself. Suppose the density fluctuation at a point $\boldsymbol{r}$ is $\delta(\boldsymbol{r})$; the number of galaxies expected

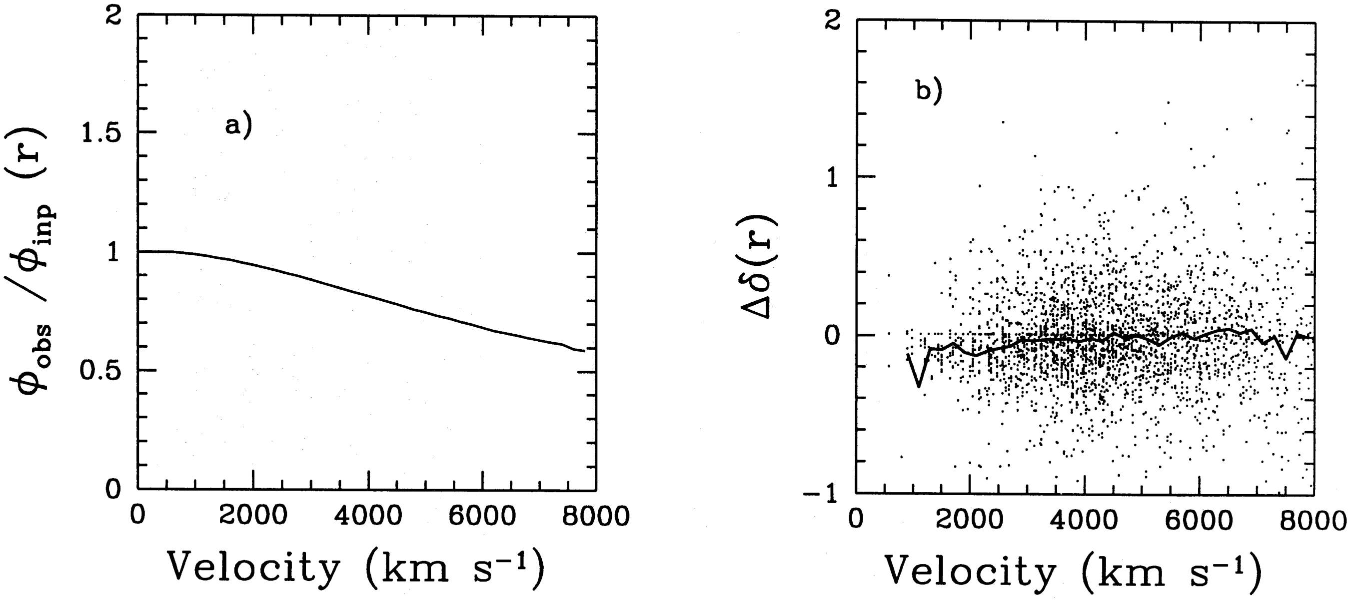

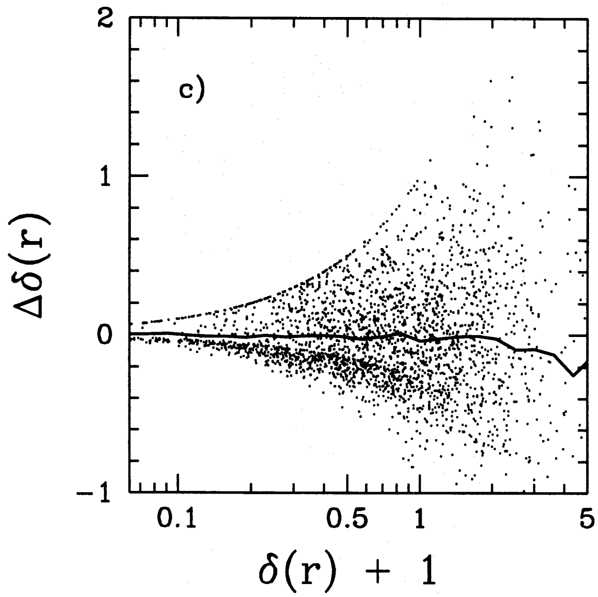

FIG. 6.—(*a*) Ratio of derived to input selection functions for a Monte Carlo simulation whose magnitudes were systematically biased according to eq. (13) in the text. (*b*) Difference between input and derived densities as a function of velocity distance. The solid line is the mean difference in distance bins. (*c*) Errors in density plotted as a function of input density.

within a neighborhood dV of $\mathbf{r}$ is[9]

$$N_{\rm obs}(\mathbf{r}) = [1 + \delta(\mathbf{r})]n_1\, dV \times \int_{L_{\rm min}'(\mathbf{r})} dL' \int_{-\infty}^{\infty} g(\epsilon,\, f)\Phi(4\pi r^2 f)d\epsilon\ ; \quad (14)$$

$L' \equiv 4\pi r^2(f + \epsilon)$ is the observed luminosity, and $4\pi r^2 f$ is the true luminosity. The observed selection function $\phi_{\rm obs}(\mathbf{r})$ is given by an integral over observed luminosities, down to $L'_{\rm min}(r)$, of the observed luminosity function. The observed luminosity function is the convolution of the true luminosity function with the error distribution function; thus

$$n_1 \phi_{\rm obs}(r) = \int_{L_{\rm min}'(\mathbf{r})}^{\infty} dL' \int_{-\infty}^{\infty} g(\epsilon,\, f)\Phi(4\pi r^2 f)d\epsilon\ , \quad (15)$$

which is the same double integral as in equation (14). Thus the observed density field is given by

$$1 + \delta_{\rm obs}(\mathbf{r}) \equiv \frac{N_{\rm obs}(\mathbf{r})}{n_1 \phi_{\rm obs}(\mathbf{r})\, dV} = 1 + \delta(\mathbf{r})\ . \quad (16)$$

Therefore, *the density field is unbiased by random errors in the fluxes.* The one assumption we made was that the error distribution was independent of position in the sky.

We demonstrate this with Monte Carlo simulations. We assume a Gaussian error distribution in magnitudes with zero mean. In Figure 7*a*, we plot the derived selection functions for two different choices of Gaussian width σ. We also plot the result for the case of σ depending on magnitude: $\sigma = 0.2$ for $m \leq 13$ and increasing linearly with m to $\sigma = 0.5$ for $m \geq 14.5$. The selection function becomes increasingly flatter (ratio increasing) with increasing σ, due to Malmquist bias. In Figures 7*b* and 7*c*, respectively, we show the mean difference between intrinsic and derived densities for each case, as a function of density and distance. No systematic differences are found as a function of distance. There is a small tendency for underdense regions to have their densities overestimated, and for overdense regions to have their densities underestimated, due to the effect of random errors, but this is at most a 10% effect for the examples shown. This confirms the robustness of the density field to random errors in the magnitudes. Finally, Figure 7*d* shows the rms error in the density field as function of the density; although the bias does not grow with increasing σ, the error certainly does.

3. ORS RESULTS

In this section we derive luminosity and diameter functions for ORS galaxies. We also discuss the amplitude of extinction effects on the data and its dependence on morphological types. Finally, we show the density field projected on several different slices of the local universe.

The three catalog from which the ORS sample was defined are based on separate plate material and were done by different observers. In anticipation of differences in the various photometric systems, we derived the selection functions separately for each catalog, for both magnitude and

---

[9] We have not included the effects of extinction, for simplicity.

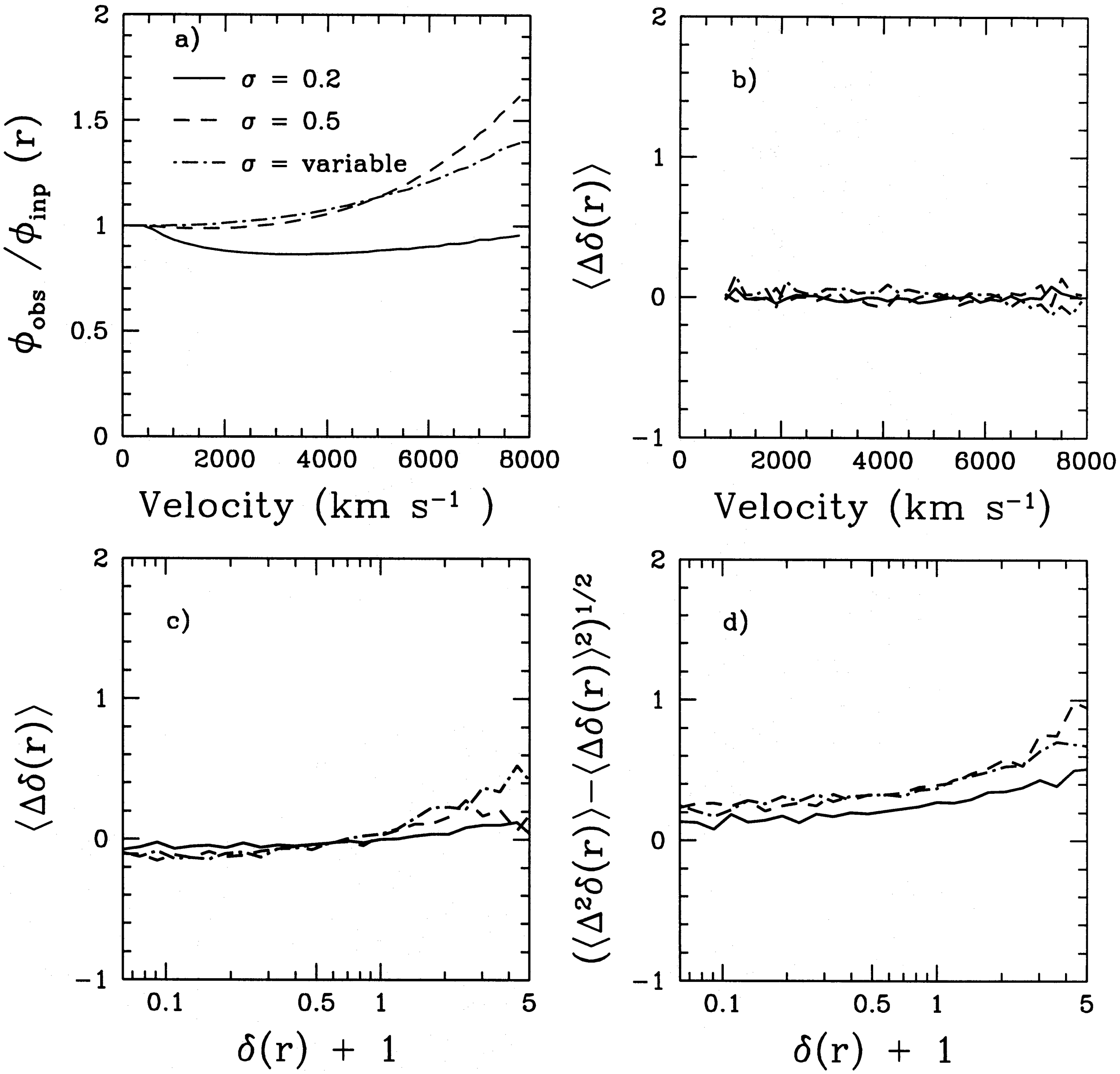

FIG. 7.—(*a*) Ratio of derived to input $\phi(r)$ for three Monte Carlo simulations whose magnitudes were subjected to random errors Gaussian distributed with standard deviations 0.2 mag (*solid line*), 0.5 mag (*dashed line*) and linearly increasing with magnitude (*dot-dashed line*). (*b*) Mean error in the density field as a function of velocity for the three Monte Carlo simulations whose selection functions are given in (*a*). (*c*) Mean error for the three simulations as a function of the input density. (*d*) Root mean square for the three simulations as a function of the input density.

diameter-limited samples. Luminosity and diameter functions then follow automatically from the inferred $\phi(r)$. As we saw in the previous sections, these are probably biased by unknown systematic and random errors internal to each catalog from which ORS was extracted. Systematic errors within each catalog's limits are difficult to quantify. There are indications, for instance, that the magnitudes from Volume 1 of the CGCG (Zwicky et al. 1961–1968) are systematically fainter by $\Delta = 0.3$ mag than those from the other volumes (Kron & Shane 1976; Paturel 1977). Instead of computing a separate selection function for this volume, we explicitly correct its magnitudes just as we do for extinction. As for random errors, they are estimated to be of approximately $\Delta m \simeq 0.09$ and $\Delta m \simeq 0.3$ for ESO and Zwicky magnitudes, respectively (Lauberts & Valentijn 1989; Kron & Shane 1976; Huchra 1976). Errors in the diameters are typically $\delta \log D \lesssim 0.09$ (Paturel et al. 1987, 1991; de Vaucouleurs et al. 1991). According to the results shown in Figure 7, the associated biases in the density field are typically not larger than 10% of the mean density. The quoted errors, however, may depend on such parameters as inclination, morphological type, or magnitudes and diameters themselves. Since our main interest is in the density field, which we found to be less vulnerable to random and systematic errors than is the luminosity function, we opted not to try to apply further corrections to the ORS selection functions besides those for extinction and for Volume 1 of CGCG.

In deriving the selection functions, we correct diameters and magnitudes for discreteness effects using the method described by Strauss, Yahil, & Davis (1991). For the ESO-m sample, we take the 1′ diameter cutoff inherent in this sample into account when deriving the selection function. This is done by substituting min $[r_{max}(L_i), r_{max}(D_i)]$ for

$r_{\max}(L_i)$ in equation (12) for the likelihood function. In all fits to $\phi(r)$, we assume that distances are proportional to redshifts in the Local Group rest frame, following Yahil, Tammann, & Sandage (1977) to convert from heliocentric velocities. Only galaxies with $r \leq 8000$ km s^{-1} are included in each fit, as the samples become unacceptably sparse at higher redshifts (cf. Fig. 4 of Paper I). Galaxies around rich clusters are placed at each cluster's center, following Table 2 of YSDH.

Each galaxy is weighted by the inverse of the product of the selection function and the mean density in each subsample, n_1. When combining samples, we multiply by a further weight given by the inverse of the relative density of *IRAS* galaxies from the 1.2 Jy redshift survey (Fisher et al. 1995) within the solid angle of each sample and within a redshift of 8000 km s^{-1}. These relative densities are 1.025 for the UGC sample, 1.233 for the ESGC sample, 0.760 for the ESO sample limited in diameter, and 0.785 for the ESO sample limited in magnitude (which covers a smaller solid angle; see Paper I).

The derived $\phi(r)$ parameters for the various samples are given in Table 1. They are labeled by the parent catalog from which they were drawn, with a suffix -d or -m for diameter and magnitude-limited samples, respectively. We also list the number of galaxies used in the maximum likelihood fit, the derived extinction correction parameter γ, and the global mean density for each sample. Formal fit errors for the $\phi(r)$ parameters typically vary from 10% to 30%. Errors for γ are larger, especially for the diameter-limited subsamples, where they can be larger than 100%! This is at least partially due to the fact that the approximation that γ_d is the same for all galaxies in the sample is not very good (cf. Fig. 1). Another factor may be systematic and random errors in the diameters, which may be of larger amplitude than the extinction effect. Of course, there is also substantial covariance between the values of the selection function parameters and γ. The ESGC-d and UGC-d subsamples have $\gamma < 0$ (extinction increases the apparent size of the galaxy), which is unphysical.

The errors in γ_m for the ESO and UGC samples are 0.28 and 0.35, respectively, consistent with the error bars in the upper panel of Figure 3. The γ-values for ESO-m and UGC-m are also consistent with unity, as expected. But how much improvement does the incorporation of extinction into the fit to $\phi(r)$ cause? The quantity $\Delta \log \Lambda$, the logarithm of the ratio of the likelihood for the best value of γ to that with γ set to zero, is shown in the last column of Table 1. The extinction corrections give a large improvement to the likelihood for ESO-m. For UGC-m, the extinction corrections may be masked by the larger errors in the Zwicky magnitudes. For the diameter-limited samples, the improvement is again small.

In Figure 8 we show the quantity $n_1\phi(r)$, the number density of galaxies in each subsample as a function of distance in the absence of inhomogeneities, for the five ORS subsamples listed in the first half of Table 1. Figure 8*a* refers to the diameter-limited subsamples, while Figure 8*b* shows the magnitude-limited subsamples. The effect of extinction is quantified by showing, in the lower two panels, the ratio of $n_1\phi$ calculated without and with extinction taken into account (the parameters in the former case are not given in the tables). For the magnitude-limited subsamples, the ϕ_{obs} are steeper than the extinction-corrected $\phi(r)$, in accordance with Figure 2*b*. For the diameter-limited subsamples, however, only ESO-d shows this behavior. Given the larger uncertainties associated with γ_d, we decided to fix $\gamma_d = 0.6$, a value appropriate for ESO and UGC galaxies (Fig. 1). The derived $\phi(r)$ parameters for these fits are listed in the second half of Table 1.

Luminosity and diameter functions are plotted in Figure 9. The units of the luminosity function are galaxies Mpc^{-3} mag^{-1}, while for the diameter function they are galaxies Mpc^{-3} (5 log D/kpc)$^{-1}$. Figure 9*a* corresponds to the diameter-limited samples and Figure 9*b* to the magnitude-limited ones. As mentioned earlier, these functions are likely to be affected by Malmquist bias. Correcting for it would work in the opposite sense to extinction corrections, making the luminosity functions steeper, but unfortunately we do not have a sufficiently accurate model of the magnitude and diameter error distribution to carry out this correction. This makes it difficult to compare the results presented here to previously published luminosity functions in the literature.

The ESO, ESGC, and UGC diameter functions are systematically displaced from one another. This is due to two effects: the fact that the ESO volume is underdense relative to the UGC (ESGC) volume by 30% (60%), as given by the *IRAS* redshift survey, and the fact that the ESO diameters are systematically larger (smaller) than the UGC (ESGC) diameters by some 25% (10%) (Paper I). If we correct for these two effects, all three diameter functions show a much improved agreement. However, the best agreement between ESO and UGC is obtained if we assume that $D_{\mathrm{ESO}} = 1.20 D_{\mathrm{UGC}}$, a slightly smaller correction than in Paper I. The corrected diameter functions are shown in Figure 9*c* for all three subsamples. Also shown (*solid line*) is the diameter

TABLE 1

ORS SELECTION FUNCTION PARAMETERS

Sample	N_g	α	β	r_* (km s^{-1})	γ	n_1[a] ($10^{-2}\ h^{-3}$ Mpc^{-3})	$\Delta \log \Lambda$
ESO-m	2170	0.40	6.25	11100	1.00	10.88	23.2
ESO-d	1614	0.39	3.19	6375	0.60	6.87	1.9
UGC-m	2965	0.36	9.38	14060	0.56	8.08	0.9
UGC-d	1848	0.33	2.83	4075	−0.32	8.60	0.5
ESGC-d	1200	0.47	5.26	9500	−0.34	18.24	0.8
ESO-d	1614	0.39	3.19	6375	0.60	6.88	1.8
UGC-d	1848	0.33	2.76	4115	0.60	9.63	−2.1
ESGC-d	1200	0.50	5.44	10565	0.60	20.20	−3.2

NOTE.—All samples limited to 8000 km s^{-1}.

[a] No global correction of density from *IRAS* applied.

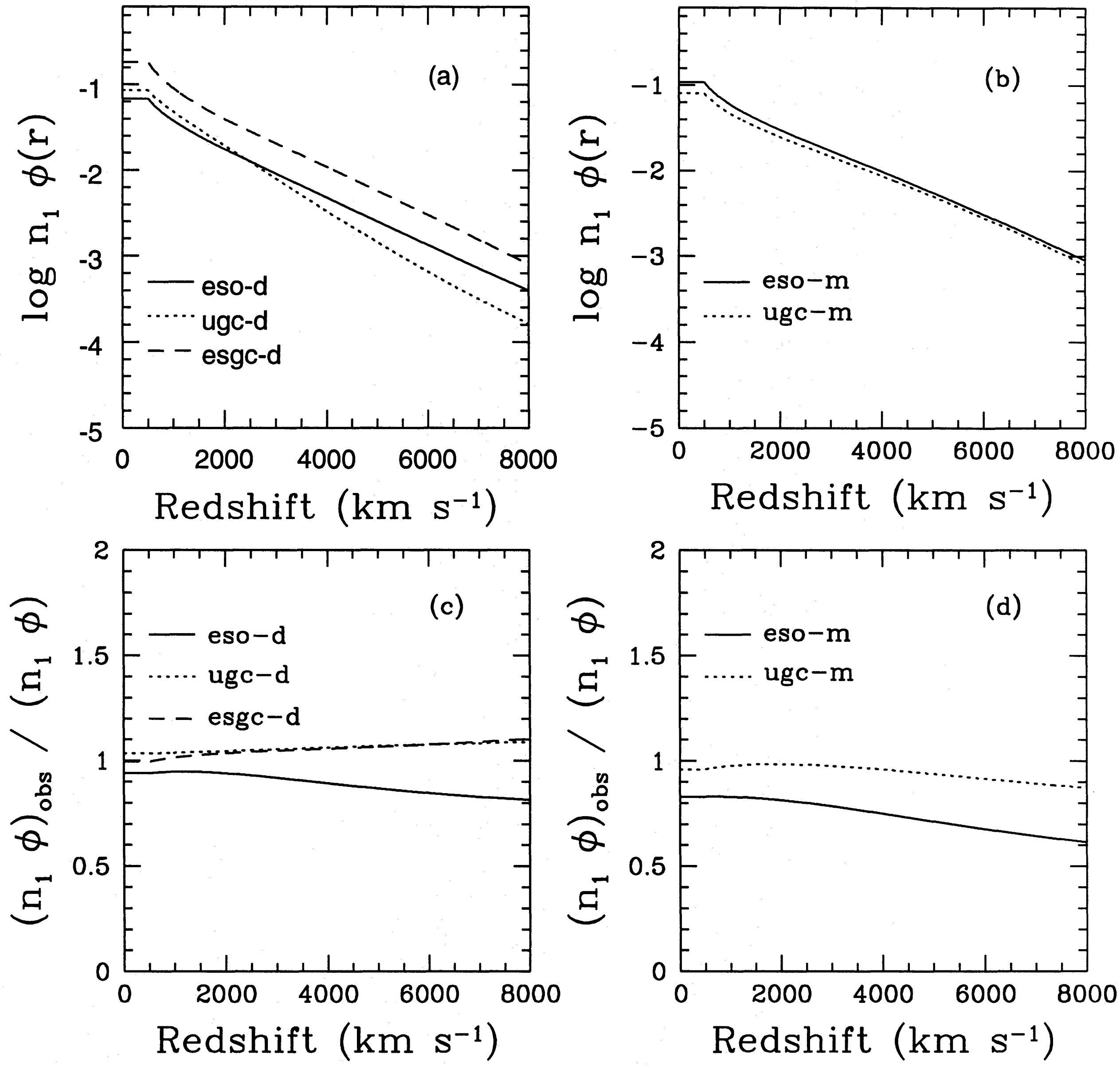

FIG. 8.—(*a*) Product of derived mean density and selection functions for the diameter-limited subsamples: ESO-d (*solid line*), UGC-d (*dotted line*), and ESGC-d (*dashed line*). (*b*) As in (*a*), for the magnitude-limited subsamples. (*c*) Ratio of the extinction-uncorrected to the extinction-corrected $n_1\phi(r)$ values for subsamples shown in (*a*). (*d*) Ratio of the extinction-uncorrected to the extinction-corrected $n_1\phi(r)$ values for subsamples shown in (*b*).

function of Hudson & Lynden-Bell (1991) derived from the CfA1 sample (Huchra et al. 1983) using UGC diameters (where we put in the same correction factor of 1.2 used for UGC-d). Notice that the revised scaling factor between ESO and UGC diameters is in closer agreement with Lynden-Bell, Lahav, & Burstein (1989). These latter also matched the UGC and ESO diameter functions and found a diameter scaling ratio of 1.17 ± 0.07, but they did not have as complete redshift information, and they did not correct for the underdensity of the ESO volume. As for the ESGC, its corrected diameter function is a bit steeper than the other two, which could be caused by residual nonlinearities in the diameters in this sample. Finally, as the Hudson & Lynden-Bell sample overlaps substantially with UGC-d, we are not surprised to find good agreement.

The agreement between the ESO and UGC luminosity functions is very good at bright magnitudes. UGC is slightly steeper on the most luminous end. However, these plots do not correct for the underdensity of ESO relative to the UGC; with this correction made, in Figure 9*d*, one can match the two luminosity functions above the knee in the luminosity functions if one assumes that the ESO magnitudes are systematically brighter by 0.2 mag than those of the UGC. However, the agreement at the low luminosity remains poor. Again, this may be a sign of residual nonlinearities in the magnitudes in one of the two samples, or perhaps differences in the corrections needed for Malmquist bias. In Figure 9*d* we also show the luminosity function derived by Loveday et al. (1992) from a sample with essentially no overlap with ours. The agreement with UGC is very good over the entire range of magnitudes, but we again had to apply an empirical shift of 0.2 mag to the Loveday et al. data.

We now discuss the quality of our best-fit solutions for the five ORS subsamples considered. As discussed by YSDH, the fit quality can be assessed by comparing the

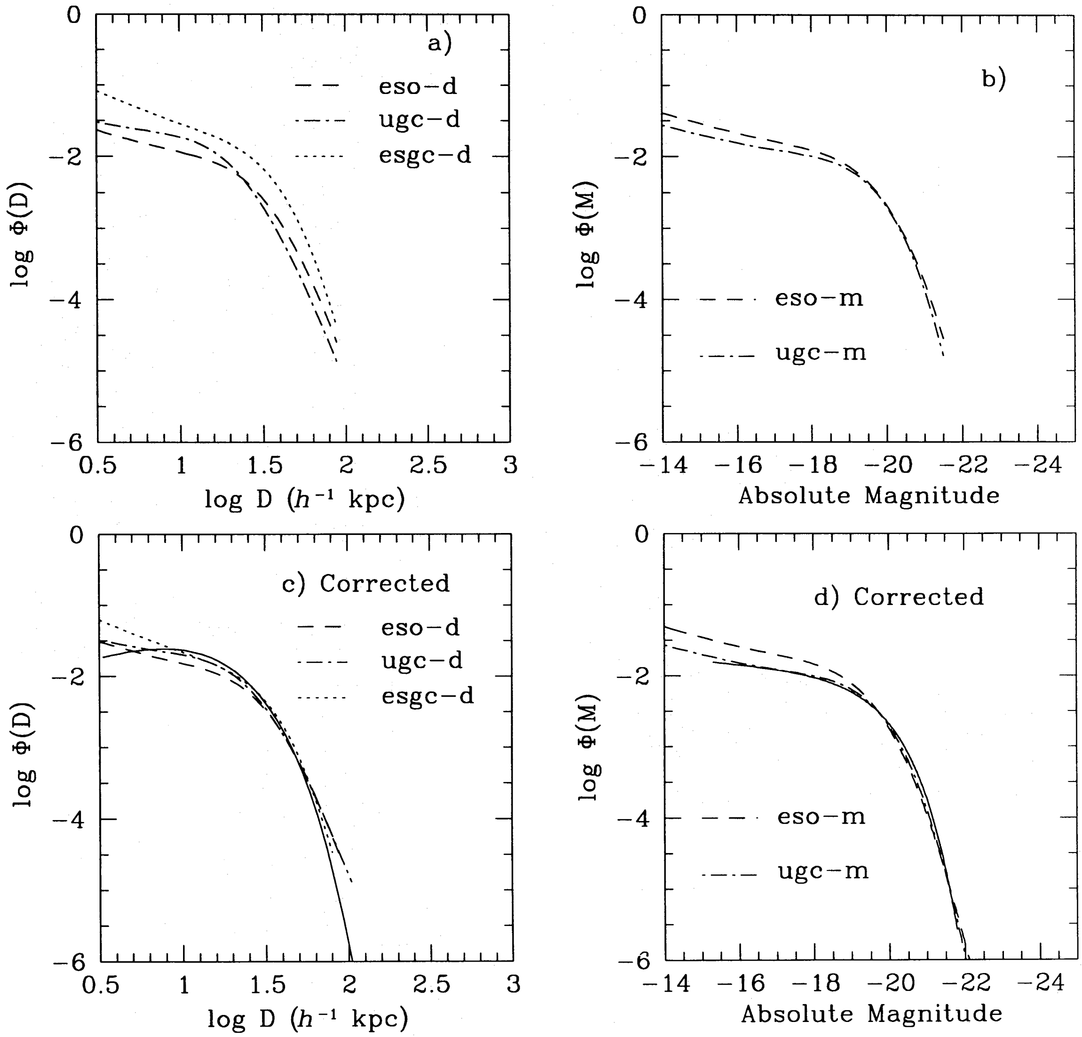

FIG. 9.—(*a*) Derived diameter functions for the ESO-d (*dashed line*), ESGC-d (*dotted line*), and UGC-d (*dot-dashed line*) subsamples. The units are galaxies Mpc^{-3} (5 log *D*/kpc)$^{-1}$. (*b*) Luminosity functions for the ESO-m (*dashed line*) and UGC-m (*dot-dashed line*) subsamples. The units are galaxies Mpc^{-3} mag^{-1}. (*c*) ESO-d, ESGC-d, and UGC-d diameter functions after taking into account the differences in mean density and diameter scale between the three samples. The solid line is the diameter function of CfA1 galaxies by Hudson & Lynden-Bell (1991). (*d*) ESO-m and UGC-m luminosity functions after taking into account the differences in mean density and magnitude scale between the two samples. The solid line is the luminosity function of Loveday et al. (1992) without any correction for Malmquist bias.

observed distribution of luminosities to that predicted from the derived $\Phi(L)$; for each galaxy at a given distance r, the predicted distribution function of luminosity is given by equation (12). Moreover, if $\Phi(L)$ is in fact universal (which is an assumption inherent in the maximum likelihood technique used) and the fitted solution is reasonable, the predicted distribution of luminosities should match that observed for any subset of the sample without explicit selection on luminosity.

The histograms in Figure 10 are the observed luminosity and diameter distributions for the five ORS subsamples considered in this paper. The smooth curves are the expected distributions given by equation (12) and the observed distribution of distances.

We quantify the difference between the observed and predicted distributions by computing the statistic

$$\frac{\chi^2}{\mathrm{dof}} = \frac{\sum_{\mathrm{bins}} (N_{\mathrm{obs}} - N_{\mathrm{pred}})^2/\sigma^2_{\mathrm{obs}}}{\mathrm{dof}}\,, \qquad (17)$$

where N_{obs} and N_{pred} are the observed and predicted number of galaxies at each bin in absolute magnitude (or diameter), respectively, dof is the number of degrees of freedom available in the comparison, and $\sigma_{\mathrm{obs}} = N^{1/2}_{\mathrm{obs}}$ is the Poisson noise in the observed counts. As in YSDH, only bins with more than five objects were used in the χ^2 determination. This quantity is shown in each panel of Figure 10 and is repeated in Table 2. The ratios are close to unity, indicating a good-quality fit.

In the remaining lines of Table 2 we show the χ^2/dof for different subsets of the data, defined according to distance, density, extinction amplitude, and morphological type. The values of χ^2/dof are in general consistent with unity. There are some exceptions, however. The large χ^2/dof for the lowest A_B range in ESO-m, for instance, could be indicative of problems in the BH extinction maps in the Southern Hemisphere. However, we would then expect a similarly poor fit in ESO-d, which is not the case. The χ^2/dof in the last distance bin of UGC-m could be due to Malmquist bias.

TABLE 2

χ^2/dof FOR THE COMPARISON BETWEEN PREDICTED AND OBSERVED LUMINOSITY (OR DIAMETER) DISTRIBUTIONS OF ORS SUBSAMPLES

Subsample	ESO-m	ESO-d	UGC-m	UGC-d	ESGC-d
All	33.6/25	37.0/25	27.0/27	27.2/28	22.5/22
$V \leq 2000$	24.1/21	41.1/21	15.6/22	24.1/22	7.6/13
$2000 \leq V \leq 4000$	14.5/15	19.8/14	17.0/15	10.6/11	17.1/12
$4000 \leq V \leq 6000$	7.5/9	5.4/9	17.9/10	1.8/10	11.4/9
$6000 \leq V \leq 8000$	9.5/7	4.6/6	29.6/8	4.6/5	8.4/6
$\delta \leq -0.5$	20.9/23	45.8/24	21.6/26	30.5/27	15.6/20
$-0.5 \leq \delta \leq 0.5$	3.5/6	2.2/2	6.8/11	1.9/6	2.7/6
$0.5 \leq \delta \leq 2.0$	7.5/12	9.2/8	19.5/14	9.8/12	14.7/7
$\delta \geq 2.0$	15.2/15	11.0/15	20.8/22	21.0/21	20.7/9
Clusters	...	...	10.0/15	20.3/11	...
$A_B \leq 0.05$	51.5/21	22.0/22	32.8/25	37.7/26	15.2/16
$0.05 \leq A_B \leq 0.10$	10.8/13	8.9/12	11.5/17	12.8/19	22.9/17
$0.10 \leq A_B \leq 0.25$	14.1/16	30.3/16	13.0/20	17.2/21	12.4/16
$0.25 \leq A_B \leq 1.00$	12.2/15	13.8/16	11.9/10	8.6/12	7.7/11
$T \leq 0$	34.3/22	13.0/17	28.0/22	9.8/19	30.4/15
$1 \leq T \leq 6$	26.5/20	40.7/19	26.1/23	31.9/22	11.6/15
$7 \leq T \leq 11$	25.0/14	34.0/16	48.8/19	26.1/20	15.3/14

There are also several large χ^2/dof values for some ranges in density which might indicate a dependence of $\Phi(L)$ on environment density. In fact, variations in $\Phi(L)$ have been found as a function of local density, usually quantified by a change in the correlation function of galaxies as a function of luminosity (Maurogordato & Lachièze-Rey 1987; Hamilton 1988; Davis et al. 1988; Bouchet et al. 1993; Park et al. 1994). This issue is, however, still subject to debate (Alimi, Valls-Gabaud, & Blanchard 1988; Valls-Gabaud, Alimi, & Blanchard 1989). Finally, several morphological subsamples show large values of χ^2/dof, indicating that the luminosity function may be a function of morphology. Again, dependence of $\Phi(L)$ on morphology has been observed by several authors (e.g., Binggeli et al. 1988; Ferguson & Sandage 1991; Santiago & Strauss 1992). Notice, however, that no systematic trends in the quality of the fits are found as a function of either extinction, density, velocity, or Hubble type, for both diameter- and magnitude-limited subsamples. Thus, we may conclude that the fits obtained to each subsample are reasonable; moreover, our data are consistent with our assumption that the luminosity and diameter functions are universal.

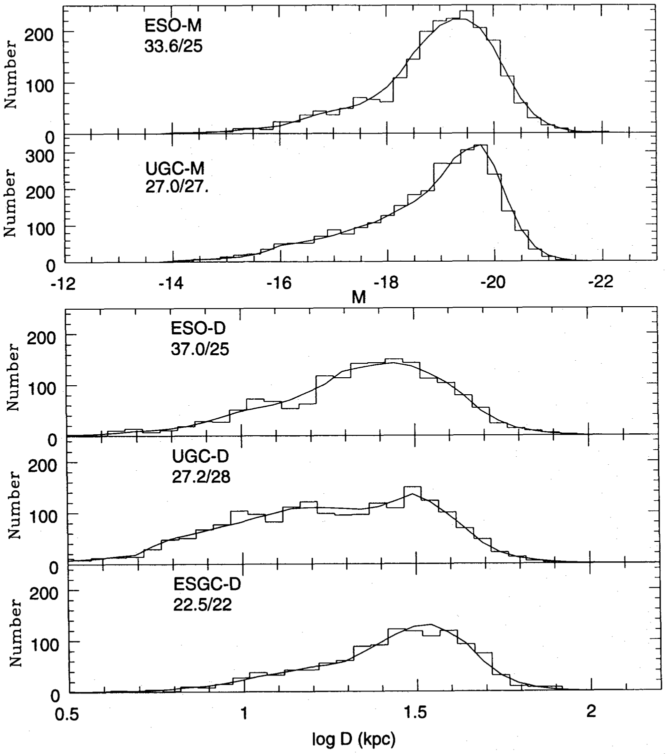

FIG. 10.—(*a*) The histogram shows the luminosity distribution of galaxies in the ESO-m subsample. The solid line is the expected distribution from the best-fit solution to $\Phi(L)$ as given in Table 1. The goodness-of-fit parameter χ^2/dof is also shown. (*b*) As in (*a*), for the UGC-m subsample. (*c*) As in (*a*), for the diameter distribution of the ESO-d subsample. (*d*) As in (*c*), for the UGC-d subsample. (*e*) As in (*c*), for the ESGC-d subsample.

Extinction corrections should also depend on morphology via differences in profile shapes as shown in § 2.2 (cf. Cameron 1990). In order to assess whether this causes systematic errors in the selection function, we derived separate $\phi(r)$ for different subsets defined according to the de Vaucouleurs numerical T types. The selection function parameters, number of galaxies, γ, and global mean densities for several morphological classes are shown in Table 3. We restrict ourselves to ESO-m and UGC-m, since we found earlier that extinction corrections for the diameter-limited samples are very uncertain.

The fits are somewhat more uncertain than those of Table 1 due to the smaller number of galaxies in each subsample. We again use the χ^2/dof statistics, listed in the last column of Table 3, to quantify the difference between observed and expected distributions. All, with the exception of the spirals in UGC-m, are close to unity. Statistical noise is particularly important for the irregulars/dwarfs subset ($7 \leq T \leq 11$), where in spite of the good fit, the formal errors in the parameters are substantial. Clear differences in the $\Phi(L)$ parameters are seen as a function of type. In particular, γ is systematically larger for late-type galaxies than for early types. Notice, however, that the errors in γ are large enough to render most values of this parameter consistent with unity. Furthermore, the existence of correlations among the parameters used in the maximum likelihood fit is also clear from Table 3. In particular, β and r_* are strongly

TABLE 3

ORS SELECTION FUNCTION PARAMETERS FOR DIFFERENT MORPHOLOGICAL TYPES

Sample	N_g	α	β	r_* (km s^{-1})	γ	n_1[a] ($10^{-2}\ h^{-3}$ Mpc^{-3})	χ^2/dof
ESO-m							
$T \le -3$	381	0.38	7.49	15540	0.51	1.07	14.2/16
$-2 \le T \le 0$	477	0.35	8.96	11880	1.01	3.09	16.8/17
$1 \le T \le 4$	801	0.20	14.71	17220	1.57	2.29	22.8/20
$5 \le T \le 6$	322	0.12	3.47	6090	1.00	0.76	11.0/20
$7 \le T \le 11$	189	−0.05	2.42	1860	3.12	4.96	12.6/15
UGC-m							
$T \le -3$	401	0.29	40.07	35670	0.42	0.57	13.9/18
$-2 \le T \le 0$	590	0.26	8.81	11520	−0.19	1.71	19.2/24
$1 \le T \le 4$	961	0.00	2.93	5190	1.00	1.16	40.9/25
$5 \le T \le 6$	680	0.33	4.85	8730	0.85	1.90	23.0/25
$7 \le T \le 11$	215	0.86	8.27	10050	0.92	9.45	15.2/21

NOTE.—All samples limited to 8000 km s^{-1}.

[a] No global correction of density from *IRAS* applied.

correlated. Figure 11 illustrates this with likelihood contours for the entire ESO-m subsample projected on the β-r_* plane (Fig. 11*a*) and the γ-r_* plane (Fig. 11*b*). The two contours delimit the 68% and 90% confidence level regions in the parameter values. The correlation between β and r_* stands out clearly; γ is also mildly correlated with r_*.

Finally, we use our best-fit solutions to the luminosity function in ESO-m, UGC-m, and ESGC in order to estimate spatial galaxy densities. In Paper I we showed density contours on constant-redshift shells; in Figure 12 we show planar slices parallel to the principal planes in supergalactic coordinates. Similar plots of the galaxy distribution have been shown by Saunders et al. (1991), Strauss et al. (1992a), Fisher et al. (1995), and Strauss & Willick (1995) for *IRAS*-selected galaxies, and Hudson (1993) for optically selected galaxies. Gaussian smoothing was used, with a width given by the mean interparticle spacing of the UGC-m sample at each distance. The zone of avoidance ($|b| < 20°$) is indicated by shading in each panel. The calculations were done to a radius of 8000 km s^{-1}, indicated by the dashed circle in each panel.

The supergalactic plane (SGZ = 0) is the central panel in the plot. Some of the more dramatic features are labeled here: the Virgo Cluster (V) is the overdensity near the origin. The Hydra-Centaurus (H-C) and Pavo-Indus-Telescopium (P-I-T) superclusters lie just above and below the zone of avoidance at SGX = −3000 km s^{-1}. The *IRAS* galaxy distribution, which continues to lower Galactic latitudes, shows these two structures to be contiguous together making up the Great Attractor. At lower SGY is the Sculptor Void (Sc). The Coma Cluster (Co) lies at SGY = 6500 km s^{-1}, SGX = 0. The Pisces-Perseus (P-P) supercluster lies largely in the zone of avoidance, although much of it is apparent at SGX = 4500 km s^{-1}, SGY = −3000 km s^{-1}; it is contiguous with the Cetus supercluster at lower SGY.

Slices 3000 km s^{-1} above and below the supergalactic plane are shown in the two panels to the right and left of the central panel, respectively. The region above the supergalactic plane is dominated by a large void and the high SGZ extension of the Great Attractor. The most prominent structure in the slice at SGZ = −3000 km s^{-1} is a part of the Great Wall (Geller & Huchra 1989) at SGX = −2000 km s^{-1}, SGY = 6000 km s^{-1}.

Slices at constant SGX are found in the upper three

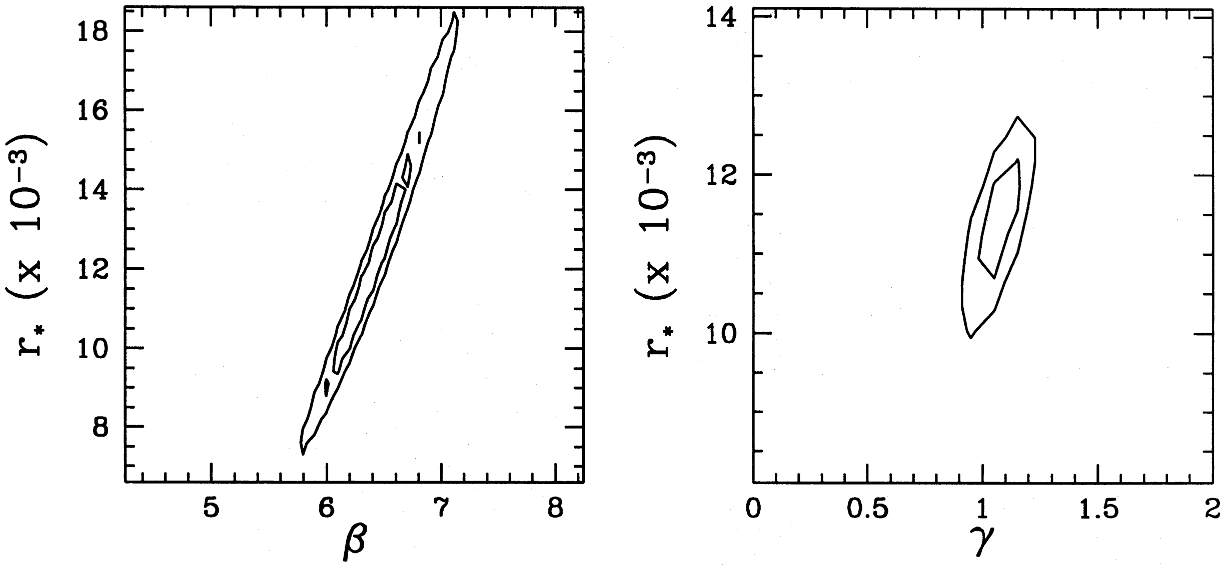

FIG. 11.—68% and 90% confidence level contours in the likelihood function of ESO-m as projected on the β-r_* plane and (*b*) on the γ-r_* plane

1996ApJ...461...38S

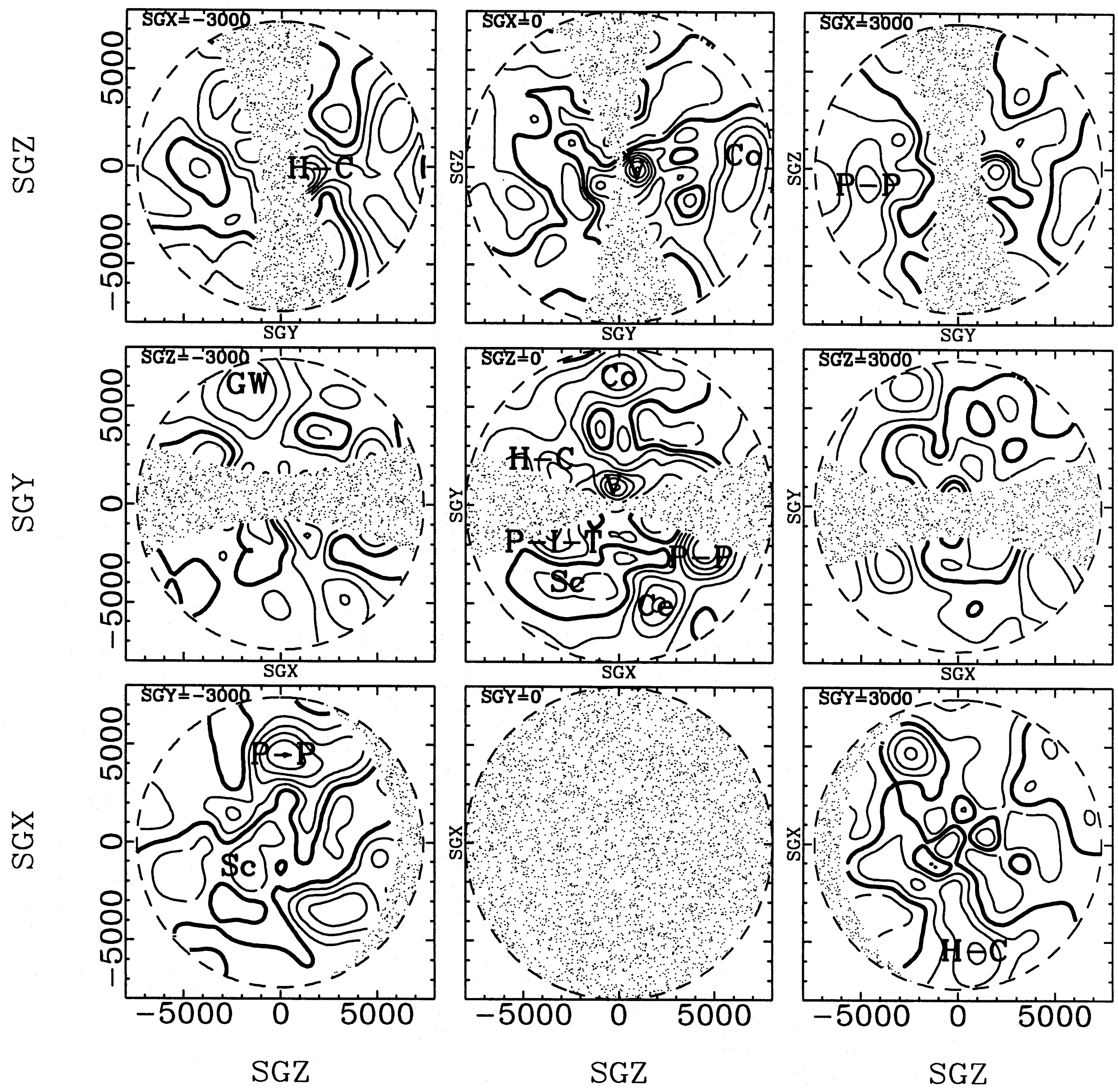

FIG. 12.—Density field of galaxies in the ORS, in nine slices parallel to the principal planes in supergalactic coordinates. The supergalactic plane is in the center with slices above and below it by 3000 km s^{-1} to the right and left, respectively. The upper panels are similar slices at constant SGX, and the lower panels are at constant SGY. Mean density is indicated by a heavy contour, and negative densities are indicated by dashed lines at $\delta = -\frac{1}{3}$ and $-\frac{2}{3}$. The zone of avoidance is indicated by shading.

panels. SGX = 0 (*center*) cuts through the Virgo and Coma clusters, while the right and left panels cut through the Pisces-Perseus and Hydra-Centaurus superclusters, respectively. Finally, the lower three panels show slices at constant SGY. SGY = 0 lies completely in the Galactic plane, and the SGY = -3000 km s^{-1} panel cuts through the southern part of the Pisces-Perseus supercluster and the Sculptor Void.

4. CONCLUSIONS

We have used Monte Carlo simulations to assess the amplitude of biases caused by different types of systematic and random errors on the derived selection function and density field of a galaxy sample. Our results may be summarized as follows:

1. Galactic extinction causes a nonuniform selection effect across the sky. The selection function derived in the usual way (as a function of radial distance only) is incapable of accounting for this effect. At best, it reflects the mean loss of galaxies averaged over all directions. The same conclusion applies to any other systematic position-dependent bias present in the magnitudes or diameters used in selecting a sample.
2. An unbiased selection function can be recovered from a redshift sample in the case of extinction by taking this effect explicitly into account. However, other (unknown) systematic as well as random errors on diameters and magnitudes interfere with extinction corrections.

3. The effect of extinction on diameters is both smaller and more variable than that on magnitudes. These two factors make it harder to incorporate extinction corrections into the selection function derivation for diameter-limited samples than for their magnitude-limited counterparts.

4. The density field is not strongly affected by systematic effects whose amplitudes do not vary across the sky, since these can still be properly incorporated into a radial selection function. Furthermore, shell densities averaged over solid angle are not biased even in the presence of errors as a function of position on the sky, since they depend on radial distance only and, as such, involve an averaging of densities taken over the entire sample solid angle.

5. Random errors also corrupt the derived selection function. As in the case of systematic errors, however, they significantly affect the density field only if their typical amplitude varies across the sky.

6. Luminosity and diameter functions are systematically biased by errors in the magnitudes and diameters, respectively. Unbiased estimates of $\Phi(L)$ and $\Phi(D)$ can be recovered only if these errors are known and corrected for when deriving the selection function. This applies to both uniform and nonuniform errors, either systematic or random.

Using the maximum likelihood technique described in § 2.2, extinction-corrected selection and luminosity functions were derived for the ORS magnitude-limited subsamples. These may, however, be biased by systematic and random errors. For the diameter-limited subsample, the effect of extinction was, as expected, harder to quantify, leading to unacceptably large uncertainties in the extinction corrections. We thus chose to apply a fixed typical extinction correction for the diameter-limited subsamples.

We derived separate selection functions for the three different catalogs from which ORS was drawn. This was done in order to circumvent biases caused by nonuniform sample selection among the three parts of the sky. For comparison, we also derived radial selection functions that completely ignore extinction. The amplitude of the extinction bias in ESO-m and UGC-m is similar to that expected from the Monte Carlo simulations. The derived selection functions were tested by comparing the observed distribution of luminosities in each sample to that predicted from the fit itself. This comparison was done for several subsets of each ORS subsample. The agreement between observed and expected distributions is good, implying consistency with the implicit assumption that $\Phi(L)$ is universal. The luminosity and diameter functions are consistent with recent determinations in the literature.

Type-dependent selection functions were derived from ESO-m and UGC-m subsamples. We find a trend of increasing γ for later morphological types. However, this result is tentative, given the covariance between the selection function parameters and γ.

Finally, the ORS density field was plotted in planes parallel to the supergalactic axes. As discussed in the previous sections, this density field is fairly unbiased by random and systematic errors, apart from position-dependent systematic trends or strong and variable scatter in the magnitudes or diameters. In the next paper of this series (Strauss et al. 1995) we will make quantitative comparisons of the density field as traced by different morphological subsets of the ORS, as well as comparisons of the density field to that of infrared-selected galaxies.

We thank Karl Fisher for his help in generating the N-body models. M. A. S. is supported at the IAS under a grant from the W. M. Keck Foundation. M. A. S. is also supported in part by NASA Astrophysical grant NAG5-2882. M. D. acknowledges support of NSF grant AST-9221540. This research has made use of the NASA/IPAC Extragalactic Database (NED), which is operated by the Jet Propulsion Laboratory, Caltech, under contract with the National Aeronautics and Space Administration. B. X. S. acknowledges a doctoral fellowship from the Conselho Nacional de Desenvolvimento Científico e Tecnológico (CNPq), and the generous hospitality of the Caltech Astronomy Department. B. X. S. and O. L. thank the Institute for Advanced Study for its invitations to visit. This work is partially based on the Ph.D. thesis of B. X. S. from Observatorio Nacional, Riode Janeiro, Brazil.

REFERENCES

Alimi, J. M., Valls-Gabaud, D., & Blanchard, A. 1988, A&A, 206, L11

Binggeli, B., Sandage, A., & Tammann, G. A. 1988, ARA&A, 26, 509

Blumenthal, G. R., Faber, S. M., Primack, J. R., & Rees, M. J. 1984, Nature, 311, 517

Bouchet, F. R., Strauss, M., Davis, M., Fisher, K. B., Yahil, A., & Huchra, J. P. 1993, ApJ, 417, 36

Burstein, D., & Heiles, C. 1982, AJ, 87, 1165

Cameron, L. M. 1990, A&A, 233, 16

Choloniewski, J. 1985, MNRAS, 214, 197

———. 1986, MNRAS, 223, 1

Cole, S., Aragón-Salamanca, A., Frenk, C. S., Navarro, J. F., & Zepf, S. E. 1994, MNRAS, 271, 781

Corwin, H. G., & Skiff, B. A. 1995, Extension to the Southern Galaxies Catalogue, in preparation

da Costa, L. N., et al. 1994, ApJ, 424, L1

Davis, M., Geller, M. J., & Huchra, J. 1978, ApJ, 221, 1

Davis, M., & Huchra, J. 1982, ApJ, 254, 437

Davis, M., Meiksin, A., Strauss, M. A., da Costa, N., & Yahil, A. 1988, ApJ, 333, L9

Dekel, A., & Rees, M. J. 1987, Nature, 326, 455

de Lapparent, V., Geller, M. J., & Huchra, J. P. 1989, ApJ, 343, 1

de Vaucouleurs, G., de Vaucouleurs, A., Corwin, H., Buta, R., Paturel, G., & Fouqué, P. 1991, Third Reference Catalogue of Bright Galaxies (New York: Springer)

Efstathiou, G., Ellis, R. S., & Peterson, B. A. 1988, MNRAS, 232, 431

Ferguson, H. C., & Sandage, A. 1991, AJ, 101, 765

Fisher, K. B., Huchra, J. P., Davis, M., Strauss, M. A., Yahil, A., & Schlegel, D. 1995, ApJS, 100, 69

Geller, M. J., & Huchra, J. P. 1989, Science, 246, 897

Hamilton, A. J. S. 1988, ApJ, 331, L59

Huchra, J. 1976, AJ, 81, 952

Huchra, J. P., Davis, M., Latham, D., & Tonry, J. 1983, ApJS, 52, 89

Hudson, M. 1993, MNRAS, 265, 43

Hudson, M. J., & Lynden-Bell, D. 1991, MNRAS, 252, 219

Kirshner, R. P., Oemler, A., & Schechter, P. L. 1979, AJ, 84, 951

Kirshner, R. P., Oemler, A., Schechter, P. L., & Shectman, S. 1983, AJ, 88, 1285

Koo, D., & Kron, R. 1992, ARA&A, 30, 613

Kron, G. E., & Shane, C. D. 1976, A&SS, 39, 401

Lahav, O., Rowan-Robinson, M., & Lynden-Bell, D. 1988, MNRAS, 234, 677

Lauberts, A. 1982, The ESO-Uppsala Survey of the ESO(B) Atlas (Garching: ESO)

Lauberts, A., & Valentijn, E. 1989, The Surface Photometry Catalogue of the ESO-Uppsala Galaxies (Garching: ESO)

Loveday, J., Peterson, B. A., Efstathiou, G., & Maddox, S. J. 1992, ApJ, 390, 338

Loveday, J., Maddox, S. J., Efstathiou, G., & Peterson, P. A. 1995, ApJ, 442, 457

Lynden-Bell, D., Lahav, O., & Burstein, D. 1989, MNRAS, 241, 325

Maia, M. A. G., & da Costa, L. N. 1990, ApJ, 352, 457

Marzke, R. O., Huchra, J. P., & Geller, M. J. 1994, ApJ, 428, 43

Maurogordato, S., & Lachièze-Rey, M. 1987, ApJ, 320, 13

Nicoll, J. F., & Segal, I. E. 1983, A&A, 118, 180

Nilson, P. 1973, Uppsala General Catalogue of Galaxies, Uppsala Astron. Obs. Ann., 6

Park, C., Vogeley, M. S., Geller, M. J., & Huchra, J. P. 1994, ApJ, 431, 569
Paturel, G. 1977, A&A, 56, 259
Paturel, G., Fouqué, P., Buta, R., & Garcia, A. M. 1991, A&A, 243, 319
Paturel, G., Fouqué, P., Lauberts, A., Valentijn, E. A., Corwin, H. G., & de Vaucouleurs, G. 1987, A&A, 184, 86
Sandage, A., Tammann, G. A., & Yahil, A. 1979, ApJ, 232, 352
Santiago, B. X., & Strauss, M. A. 1992, ApJ, 387, 9
Santiago, B. X., Strauss, M. A., Lahav, O., Davis, M., Dressler, A., & Huchra, J. P. 1995, ApJ, 446, 457 (Paper I)
Saunders, W., Frenk, C., Rowan-Robinson, M., Efstathiou, G., Lawrence, A., Kaiser, N., Ellis, R., Crawford, J., Xia, X. Y., & Parry, I. 1991, Nature, 349, 32
Schechter, P. L. 1976, ApJ, 203, 297
Sodré, L., & Lahav, O. 1993, MNRAS, 260, 285
Strauss, M. A., Davis, M., Yahil, A., & Huchra, J. P. 1990, ApJ, 361, 49
———. 1992a, ApJ, 385, 421
Strauss, M. A., Huchra, J. P., Davis, M., Yahil, A., Fisher, K. B., & Tonry, J. 1992b, ApJS, 83, 29
Strauss, M. A., & Willick, J. 1995, Phys. Rep., in press
Strauss, M. A., Yahil, A., Davis, M., Huchra, J. P., & Fisher, K. B. 1992c, ApJ, 397, 395
Strauss, M. A., Yahil, A., & Davis, M. 1991, PASP, 103, 1012
Strauss, M. A., et al. 1995, in preparation (Paper III)
Turner, E. L. 1979, ApJ, 231, 645
Valls-Gabaud, D., Alimi, J. M., & Blanchard, A. 1989, Nature, 341, 215
White, S. D. M., & Frenk, C. S. 1991, ApJ, 379, 52
Yahil, A. 1988, in Large Scale Motions in the Universe: A Vatican Study Week, ed. V. C. Rubin, & G. V. Coyne, S.J. (Princeton: Princeton Univ. Press), p. 219
Yahil, A., Strauss, M. A., Davis, M., & Huchra, J. P. 1991, ApJ, 372, 380 (YSDH)
Yahil, A., Tammann, G. A., & Sandage, A. 1977, ApJ, 217, 903
Zwicky, F., et al. 1961–1968, Catalog of Galaxies and Clusters of Galaxies, Vols. 1–6 (Pasadena: Caltech) (CGCG)